Satellite Data Assimilation in Numerical Weather Prediction Models. Part I: Forward Radiative Transfer and Jacobian Modeling in Cloudy Atmospheres

FUZHONG WENG

Joint Center for Satellite Data Assimilation, and NOAA/NESDIS/Office of Research and Applications, Camp Springs, Maryland

QUANHUA LIU

Joint Center for Satellite Data Assimilation, Camp Springs, Maryland, and Cooperative Institute for Research in the Atmosphere, Colorado State University, Fort Collins, Colorado

(Manuscript received 30 September 2002, in final form 1 May 2003)

ABSTRACT

Satellite data assimilation requires rapid and accurate radiative transfer and radiance gradient models. For a vertically stratified scattering and emitting atmosphere, the vector discrete-ordinate radiative transfer model (VDISORT) was developed to derive all Stokes radiance components at the top of the atmosphere. This study further enhances the VDISORT to compute the radiance gradients or Jacobians. The band matrix used in the VDISORT is simplified and confined along the diagonal direction so that the Jacobians relative to atmospheric and surface parameters are directly derived from its analytic solutions. The radiances and Jacobians at various wavelengths from the VDISORT are compared against those from other techniques that have been benchmarked before. It is shown that the present method is accurate and computationally efficient.

In the VDISORT, both emissivity vector and reflectivity matrix are integrated as part of the radiance and Jacobian calculations. In this study, only the emissivity models at microwave frequencies are tested and implemented for VDISORT applications. Over oceans, a full polarimetric emissivity model is utilized. The cutoff wavenumber separating the large-scale waves from the small-scale waves is derived from an ocean wave spectrum model. Over land, a microwave emissivity model previously developed is used to compute various emissivity spectra.

1. Introduction

A computationally efficient and accurate radiative transfer model is needed for radiance and Jacobian calculations in satellite data assimilation. Presently, the model used in numerical weather prediction (NWP) models does not take into account the scattering and polarization. In the absence of scattering, the components used in data assimilation systems such as atmospheric transmittance and the gradient of radiance relative to a state variable are parameterized (Garand et al. 2001) or derived analytically (Eyre 1989). Thus, the radiance measurements from satellites under clear atmospheres have been most successfully assimilated into global NWP models.

To fully utilize the information of satellite measurements under all weather conditions for numerical weather prediction, we need to enhance the forward and Jacobian models by including the scattering and polarization processes. Presently, satellite cloudy radiances have not been assimilated into operational forecasting models although the measurements contain rich information on various weather processes. In the next decade when many advanced microwave and infrared sensors are deployed in space and their sensitivity to various atmospheric and surface parameters are further improved, the uses of cloudy radiances in NWP models will ultimately augment the impacts that have already been demonstrated through the clear radiance assimilation.

Currently, the advanced radiative transfer models including scattering and polarization have not been optimally developed for satellite data assimilation. The discrete-ordinate radiative transfer method (DISORT) was developed using versatile numerical packages that solve the general and particular solutions (Stamnes et al. 1988). Recently, the DISORT was expanded to also solve the Stokes vector radiative transfer problems, was named VDISORT (Weng 1992; Schulz et al. 1999; Schulz and Stamnes 2000) and included scattering and polarization at all wavelengths. The DISORT is also linearized to calculate efficiently the weighting function that may be directly used in the data assimilation (Spurr et al. 2001; van Oss and Spurr 2002). Other schemes, including the doubling–adding model (Evans and Stephens 1991) and the matrix operator method (Liu and

Corresponding author address: Dr. Fuzhong Weng, NOAA/NESDIS, Room 7006, 5200 Auth Road, Camp Springs, MD 20746.
E-mail: Fuzhong.Weng@noaa.gov

Ruprecht 1996), were also developed with a similar capability. However, in the above-mentioned schemes, efficient procedures of computing cloud optical parameters (e.g., phase matrix, scattering, and absorption coefficients) and surface optical properties (e.g., emissivity vector and reflectivity matrix) have not been integrated as part of the model developments.

The radiance gradient can be derived in a mathematically elegant way through a perturbation analysis (Marchuk 1964; Box et al. 1988). In doing so, the solutions of the forward and adjoint differential and integral equations are derived at a basic state, and the perturbation of the transport operator and source terms is then computed for a given perturbed variable. Currently, the solution of the adjoint radiative transfer equation was applied for certain boundary conditions (Sendra and Box 2000; Ustinov 2001; Landgraf et al. 2002). The techniques are yet to be proved for more general applications.

This study is the first of our series of developments in satellite data assimilation in cloudy atmospheres. We begin with a new formulation of a generalized radiative transfer scheme that allows for efficient computations of the Stokes vector and its Jacobian under cloudy conditions. In the next section, we briefly review the variational technique used for satellite radiance assimilation. The VDISORT is then improved in the boundary conditions for simultaneously deriving radiances and Jacobians. In section 3, the accuracy and efficiency of the radiances derived from the current model are compared with those from the doubling–adding model, whereas the Jacobians are compared with those from the finite differential method. As an important component in the radiance and Jacobian calculations, the surface emissivity model is presented in section 4.

2. Satellite radiance assimilation

a. Variational analysis

A novel approach in deriving atmospheric and surface parameters via the satellite data assimilation method is to use both satellite measurements and an initial guess through a variational analysis. Specifically, assuming that the errors in the observations and in the a priori information are unbiased, uncorrelated, and have Gaussian distributions, the best estimate of $\mathbf{x}$ will minimize the cost function:

$$J = \frac{1}{2}(\mathbf{x} - \mathbf{x}^b)^{\mathrm{T}}\mathbf{B}^{-1}(\mathbf{x} - \mathbf{x}^b) + \frac{1}{2}[\mathbf{I}(\mathbf{x}) - \mathbf{I}^0]^{\mathrm{T}}(\mathbf{E} + \mathbf{F})^{-1}[\mathbf{I}(\mathbf{x}) - \mathbf{I}^0], \quad (1a)$$

where $\mathbf{B}$ is the error covariance matrix associated with the background state variable $\mathbf{x}^b$; $\mathbf{E}$ and $\mathbf{F}$ are the error matrices associated with observations and forward models, respectively; $\mathbf{I}$ is the radiance vector simulated for a set of channels (or frequencies) at the state variable $\mathbf{x}$; and $\mathbf{I}^0$ is the observed radiance vector.

The minimum of the cost function is found from an iterative process that computes a descent direction at the state $\mathbf{x}$. The value of the cost-function gradient at each iteration is derived as

$$\nabla_x J = \mathbf{B}^{-1}(\mathbf{x} - \mathbf{x}^b) + \mathbf{H}^{\mathrm{T}}(\mathbf{E} + \mathbf{F})^{-1}[\mathbf{I}(\mathbf{x}) - \mathbf{I}^0], \quad (1b)$$

where $\mathbf{H}^{\mathrm{T}}$ is the adjoint operator of the Jacobian matrix $\mathbf{H}$, which is the derivative of the radiance with respect to the input variables (e.g., $\partial\mathbf{I}/\partial\mathbf{x}$).

Equations (1a) and (2b) represent the typical satellite data assimilation scheme implemented in the current numerical weather prediction models. The tangent-linear and adjoint technique allows for avoiding an explicit computation of Jacobians in the data assimilation model. The tangent-linear operator of a forward model analytically computes output perturbations corresponding to the input perturbations with a computational cost typically only about twice as much as that of the forward model. A first order of Taylor approximation is used. The adjoint of the tangent-linear operators analytically computes the sensitivity with respect to the inputs from the sensitivity with respect to the outputs (Errico 1997).

Other methods were developed to directly calculate the Jacobian matrix. Ustinov (2001) formulated an explicit Jacobian form via

$$\frac{d\mathbf{I}}{d\mathbf{x}_i} = \left(\mathbf{I}^*, \frac{d\mathbf{S}}{d\mathbf{x}_i} - \frac{dL}{d\mathbf{x}_i}\mathbf{I}\right), \quad (2)$$

where $\mathbf{I}^*$ is the solution of the adjoint radiative transfer equation, and $\mathbf{S}$ and L are the source term and the operator in the forward model, respectively. Spurr et al. (2001) also directly analyzed the perturbation components in the solution of the discrete ordinate model (Stamnes et al. 1988) and found a fast way to compute the Jacobian matrix under a generalized condition including scattering and surface reflection.

b. Radiative transfer modeling using a discrete-ordinate method

For a plane-parallel atmosphere, the radiance vector in Eqs. (1a) and (1b) can be derived from

$$\mu\frac{d\mathbf{I}(\tau, \mu, \phi)}{d\tau} = -\mathbf{I}(\tau, \mu, \phi) + \frac{\varpi}{4\pi}\int_0^{2\pi}\int_{-1}^{1}\mathbf{M}(\tau; \mu, \phi; \mu', \phi')\mathbf{I}(\tau, \mu', \phi')\,d\mu'\,d\phi' + \mathbf{S}(\tau, \mu, \phi; \mu_0, \phi_0) \quad (3a)$$

and

$$\mathbf{S} = (1 - \varpi)B[T(\tau)]\begin{bmatrix}1\\0\\0\\0\end{bmatrix} + \frac{\varpi F_0}{4\pi}\exp\left(-\frac{\tau}{\mu_0}\right)\begin{bmatrix}M_{11}(\mu, \phi; \mu_0, \phi_0)\\M_{12}(\mu, \phi; \mu_0, \phi_0)\\M_{13}(\mu, \phi; \mu_0, \phi_0)\\M_{14}(\mu, \phi; \mu_0, \phi_0)\end{bmatrix}, \tag{3b}$$

where $\mathbf{M}$ is the phase matrix, $\mathbf{I} = [I, Q, U, V]^{\Gamma}$, $B(T)$ the Planck function at a temperature T, F_0 the solar spectral constant, μ_0 the cosine of sun zenith angle, ϖ the single scattering albedo, and τ the optical thickness.

Equation (3) can be solved by some standard routines such as the multilayer discrete-ordinate method (Weng 1992; Schulz et al. 1999), the doubling–adding method (Evans and Stephens 1991), and the matrix operator method (Liu and Ruprecht 1996). Essentially, the azimuthal dependence of Stokes vector is expanded into a series of Fourier harmonics. The amplitude of each Fourier component is a function of zenith angle. Furthermore, the amplitude is discretized at a series of zenith angles (or streams) so that the combined Stokes cosine and sine harmonics can be simplified as

$$\mu_i\frac{d}{d\tau}\begin{bmatrix}\mathbf{I}_m(\tau, \mu_i)\\-\mathbf{I}_m(\tau, \mu_{-i})\end{bmatrix} = \begin{bmatrix}\mathbf{I}_m(\tau, \mu_i)\\\mathbf{I}_m(\tau, \mu_{-i})\end{bmatrix} - \varpi\sum_{j=1}^{N}\begin{bmatrix}\mathbf{M}_m(\mu_i, \mu_j) & \mathbf{M}_m(\mu_i, \mu_{-j})\\\mathbf{M}_m(\mu_{-i}, \mu_j) & \mathbf{M}_m(\mu_{-i}, \mu_{-j})\end{bmatrix}\begin{bmatrix}\mathbf{I}_m(\tau, \mu_j)\\\mathbf{I}_m(\tau, \mu_{-j})\end{bmatrix}w_j - \begin{bmatrix}\mathbf{S}_m(\tau, \mu_i, \mu_0)\\\mathbf{S}_m(\tau, \mu_{-i}, \mu_0)\end{bmatrix}, \tag{4}$$

where μ_i and w_i are Gaussian quadrature points and weights, respectively. Note that $\mu_{-i} = -\mu_i$ and $w_{-i} = w_i$. According to the properties of the phase matrix, the radiance components at sinusoidal and cosinusoidal modes can be decoupled, recombined, and solved independently (Weng 1992; see appendix A). Therefore, for each harmonic component, Eq. (4) is expressed as

$$\frac{d\mathbf{I}}{d\tau} = \mathbf{A}\mathbf{I} - \mathbf{S}, \tag{5}$$

where

$$\mathbf{I} = [\mathbf{I}(\tau, \mu_1), \mathbf{I}(\tau, \mu_2), \ldots, \mathbf{I}(\tau, \mu_N), \mathbf{I}(\tau, \mu_{-1}), \mathbf{I}(\tau, \mu_{-2}), \ldots, \mathbf{I}(\tau, \mu_{-N})]^{\mathrm{T}}, \tag{6}$$

$$\mathbf{S} = (1 - \varpi)B(T)\delta_{m0}\begin{bmatrix}\mathbf{u}^{-1} & \mathbf{0}\\\mathbf{0} & -\mathbf{u}^{-1}\end{bmatrix}\boldsymbol{\Xi} + \frac{\varpi F_0}{\pi}\exp\left(-\frac{\tau}{\mu_0}\right)\boldsymbol{\Psi}, \tag{7}$$

where $\mathbf{u}$ is a 4N by 4N matrix that has nonzero elements at its diagonal direction such as

$$\mathbf{u} = [\mu_1, \mu_1, \mu_1, \mu_1, \mu_2, \ldots, \mu_N, \mu_N, \mu_N, \mu_N]_{\text{diagonal}}, \tag{8a}$$

$\boldsymbol{\Xi}$ and $\boldsymbol{\Psi}$ are vectors that have 8N elements

$$\boldsymbol{\Xi} = [1, 0, 0, 0, 1, 0, 0, 0, \ldots, 1, 0, 0, 0]^{\mathrm{T}} \quad \text{and} \tag{8b}$$

$$\boldsymbol{\Psi} = [M_{11}(\mu_1, \mu_0)/\mu_1, M_{12}(\mu_1, \mu_0)/\mu_1, M_{13}(\mu_1, \mu_0)/\mu_1, M_{14}(\mu_1, \mu_0)/\mu_1, M_{11}(\mu_2, \mu_0)/\mu_2, M_{12}(\mu_2, \mu_0)/\mu_2, M_{13}(\mu_2, \mu_0)/\mu_2, M_{14}(\mu_2, \mu_0)/\mu_2, \ldots, M_{11}(\mu_{-N}, \mu_0)/\mu_{-N}, M_{12}(\mu_{-N}, \mu_0)/\mu_{-N}, M_{13}(\mu_{-N}, \mu_0)/\mu_{-N}, M_{14}(\mu_{-N}, \mu_0)/\mu_{-N}], \tag{8c}$$

and the composite phase matrix

$$\mathbf{A} = \begin{bmatrix}\mathbf{u}^{-1} & 0\\0 & -\mathbf{u}^{-1}\end{bmatrix}\begin{bmatrix}\mathbf{E} - \varpi\mathbf{M}(u, u) & \varpi\mathbf{M}(u, -u)\\\varpi\mathbf{M}(-u, u) & \mathbf{E} - \varpi\mathbf{M}(-u, -u)\end{bmatrix} = \begin{bmatrix}\boldsymbol{\alpha}_1 & \boldsymbol{\beta}_1\\-\boldsymbol{\beta}_2 & -\boldsymbol{\alpha}_2\end{bmatrix}, \tag{8d}$$

where $\mathbf{E}$ is a unit matrix. For a pair of zenith angles (μ_i, μ_j), both $\boldsymbol{\alpha}$ and $\boldsymbol{\beta}$ are 4N by 4N matrices and related to the elements of the phase matrices as

$$\boldsymbol{\alpha}_1(\mu_i, \mu_j) = [\mathbf{E} - \varpi\mathbf{M}_m(\mu_i, \mu_j)]/\mu_i, \tag{9a}$$

$$\boldsymbol{\beta}_1(\mu_i, \mu_{-j}) = \varpi\mathbf{M}_m(\mu_i, \mu_{-j})/\mu_i, \tag{9b}$$

$$\boldsymbol{\alpha}_2(\mu_{-i}, \mu_{-j}) = [\mathbf{E} - \varpi\mathbf{M}_m(\mu_{-i}, \mu_{-j})]/\mu_i, \tag{9c}$$

$$\boldsymbol{\beta}_2(\mu_{-i}, \mu_j) = \varpi\mathbf{M}_m(\mu_{-i}, \mu_j)/\mu_i. \tag{9d}$$

Equation (5) is a linear differential system and its solution within a homogeneous layer labeled as l can be written as

$$\mathbf{I}_l(\tau) = \exp[\mathbf{A}_l(\tau - \tau_{l-1})]\mathbf{c}_l + \mathbf{s}_l(\tau), \tag{10}$$

with

$$\mathbf{s}_l(\tau) = \delta_{m0}\left\{B(\tau_{l-1})\boldsymbol{\Xi} + \frac{B(\tau_l) - B(\tau_{l-1})}{\tau_l - \tau_{l-1}} \times [\mathbf{A}_l^{-1}\boldsymbol{\Xi} + (\tau - \tau_{l-1})\boldsymbol{\Xi}]\right\} + \mu_0[\mu_0\mathbf{A}_l + \mathbf{E}]^{-1}\frac{\varpi F_0}{\pi}\exp\left(-\frac{\tau}{\mu_0}\right)\boldsymbol{\Psi}, \tag{11}$$

for a thermal source that linearly varies with optical thickness as

$$B(\tau) = B(\tau_{l-1}) + \frac{B(\tau_l) - B(\tau_{l-1})}{\tau_l - \tau_{l-1}}(\tau - \tau_{l-1}), \quad (12)$$

where τ_l and τ_{l-1} are the optical depths at the bottom and top of the layer. Note that the coefficients vector $\mathbf{c}_l$ (8N elements in each layer) in Eq. (10) can be determined from the continuity condition of the internal boundary,

$$\mathbf{I}_l(\tau_{l-1}) = \mathbf{I}_{l-1}(\tau_{l-1}), \quad (13a)$$

as well as the external boundary at the top of the atmosphere,

$$\bar{\mathbf{I}}_1(0) = 0, \quad (13b)$$

and at the surface

$$\bar{\bar{\mathbf{I}}}_L(\tau_L) = \boldsymbol{\epsilon} B(T_s) + \mathbf{R}\bar{\mathbf{I}}_L(\tau_L) + \mathbf{R}_0 \frac{F_0}{\pi} \exp\left(-\frac{\tau_L}{\mu_0}\right)\bar{\bar{\boldsymbol{\Xi}}}, \quad (13c)$$

where $\boldsymbol{\epsilon}$ is the surface emissivity vector (4N elements), $\mathbf{R}$ is the surface reflection matrix (4N by 4N), $\mathbf{R}_0$ is the surface reflection vector (4N) at the sun zenith angle, and T_s is the surface temperature. The bar over a vector or matrix represents the continuity required at all downward zenith angles, whereas the double bars mean the continuity at all upward angles.

Substituting Eq. (10) into Eqs. (13a)–(13c) results in a set of algebraic equations for solving the coefficient $\mathbf{c}_l$ such that

$$\mathbf{PC} = \mathbf{V}, \quad (14)$$

where

$$\mathbf{P} = \begin{bmatrix}
\bar{\mathbf{E}} & \bar{\mathbf{0}} & \bar{\mathbf{0}} & \bar{\mathbf{0}} & \bar{\mathbf{0}} & \bar{\mathbf{0}} & \bar{\mathbf{0}} & \bar{\mathbf{0}} & \bar{\mathbf{0}} \\
\mathbf{e}_1 & -\mathbf{E} & \mathbf{0} & \mathbf{0} & \mathbf{0} & \mathbf{0} & \mathbf{0} & \mathbf{0} & \mathbf{0} \\
\mathbf{0} & \mathbf{e}_2 & -\mathbf{E} & \mathbf{0} & \mathbf{0} & \mathbf{0} & \mathbf{0} & \mathbf{0} & \mathbf{0} \\
\mathbf{0} & \mathbf{0} & \cdots & \cdots & \cdots & \cdots & \cdots & \cdots & \mathbf{0} \\
\mathbf{0} & \mathbf{0} & \cdots & \mathbf{e}_{l-1} & -\mathbf{E} & \cdots & \cdots & \cdots & \mathbf{0} \\
\mathbf{0} & \mathbf{0} & \cdots & \cdots & \mathbf{e}_l & -\mathbf{E} & \cdots & \cdots & \mathbf{0} \\
\mathbf{0} & \cdots & \cdots & \cdots & \cdots & \cdots & \cdots & \cdots & \mathbf{0} \\
\mathbf{0} & \mathbf{0} & \mathbf{0} & \cdots & \cdots & \cdots & \mathbf{e}_{L-2} & -\mathbf{E} & \mathbf{0} \\
\mathbf{0} & \mathbf{0} & \mathbf{0} & \mathbf{0} & \mathbf{0} & \mathbf{0} & \mathbf{0} & \mathbf{e}_{L-1} & -\mathbf{E} \\
\bar{\mathbf{0}} & \bar{\mathbf{0}} & \bar{\mathbf{0}} & \bar{\mathbf{0}} & \bar{\mathbf{0}} & \bar{\mathbf{0}} & \bar{\mathbf{0}} & \bar{\mathbf{0}} & \bar{\bar{\mathbf{E}}}\mathbf{e}_L - \mathbf{R}\bar{\mathbf{E}}\mathbf{e}_L
\end{bmatrix}, \quad (15)$$

$$\mathbf{C} = [\mathbf{c}_1, \mathbf{c}_2, \ldots, \mathbf{c}_{L-1}, \mathbf{c}_L]^{\mathrm{T}}, \quad (16)$$

$$\mathbf{V} = \left[\bar{\mathbf{E}}\mathbf{s}_1(0), \mathbf{s}_2(\tau_1) - \mathbf{s}_1(\tau_1), \ldots, \mathbf{s}_L(\tau_{L-1}) - \mathbf{s}_{L-1}(\tau_{L-1}), \epsilon B(T_s)\delta_{om} + \mathbf{R}\bar{\mathbf{E}}\mathbf{s}_L(\tau_L) + \mathbf{R}_0\mu_0\frac{F_0}{\pi}\exp\left(-\frac{\tau_L}{\mu_0}\right)\bar{\bar{\boldsymbol{\Xi}}} - \bar{\bar{\mathbf{E}}}\mathbf{s}_L(\tau_L)\right]^{\mathrm{T}}, \quad (17)$$

where $\mathbf{E}$ and $\underline{\mathbf{0}}$ are unit and zero matrices (8N by 8N), respectively; $\bar{\mathbf{0}}$ is a matrix with all elements of zero (4N $\times$ 8N); $\bar{\mathbf{E}}$ and $\bar{\bar{\mathbf{E}}}$ are the matrices corresponding to the upper and lower 4N rows in $\mathbf{E}$, respectively; and

$$\mathbf{e}_l = \exp[\mathbf{A}_l(\tau_l - \tau_{l-1})]. \quad (18)$$

For a vertically stratified atmosphere with a total of L layers, a total of 8N by L equations are coupled to derive all coefficients. Since $\mathbf{P}$ in Eq. (15) is a band matrix, the storage for its elements in computer memory can be optimally designed for speeding up the numerical calculations (Stamnes et al. 1988). This formulation also allows for the derivations of radiance gradient (or Jacobian) in an analytic form as discussed in the next section.

c. Radiance gradient computed from VDISORT

Since the radiance solution from the VDISORT is analytic in form, the Jacobian can also be explicitly obtained from Eq. (10). At the top of the atmosphere [$e^{\mathbf{A}(\tau-\tau_0)} = 1$, $l = 1$], the radiance gradient corresponding to a geophysical parameter (x_l) at the lth layer can be expressed as

$$\frac{\partial \mathbf{I}_1}{\partial x_l} = \frac{\partial \mathbf{c}_1}{\partial x_l} + \delta_{1l}\frac{\partial \mathbf{s}_1}{\partial x_l}, \quad (19)$$

where the second term on the right-hand side of Eq. (19) can be carried out directly from Eq. (11). Thus, the complexity of the Jacobians is largely dependent on

the derivative of the coefficient matrix relative to x_l. From Eq. (14),

$$\frac{\partial \mathbf{C}}{\partial x_l} = \mathbf{K}\left[\frac{\partial \mathbf{V}}{\partial x_l} - \frac{\partial \mathbf{P}}{\partial x_l}\mathbf{C}\right], \tag{20}$$

where $\mathbf{K} = \mathbf{P}^{-1}$. Manipulating Eqs. (10) and (20) results in

$$\frac{\partial \mathbf{I}_1(\mu)}{\partial x_l} = \sum_{k=l}^{L}\sum_{j=-4N}^{4N} \mathbf{K}_k(\mu, j)\left\{\frac{\partial[\mathbf{s}_k(\tau) - \mathbf{s}_{k-1}(\tau)]}{\partial x_l}\bigg|_{\tau=\tau_{l-1}}\right\}_j + \delta_{1l}\frac{\partial \mathbf{s}_1(\mu)}{\partial x_l} - \sum_{j=-4N}^{4N} \mathbf{K}_l(\mu, j)\left\{\frac{\partial}{\partial x_l}\exp[\mathbf{A}_l(\tau - \tau_{l-1})]|_{\tau=\tau_l}\mathbf{c}_l\right\}_j, \tag{21a}$$

where the subscript index j outside the bracket { } represents the jth element of the vector; $\mathbf{K}_l(\mu, j)$ is a vector at the lth layer. The first summation in the first term is the effect of the perturbation of the geophysical parameter (x_l) on the direct solar radiation. The derivatives on the right-hand side of Eq. (21a) can be directly derived using Eqs. (8d) and (11). Note that Eq. (20) is valid only for the layers above the surface. For the layer adjacent to the surface, the derivative includes more terms due to the surface reflection such that

$$\frac{\partial \mathbf{I}_1(\mu)}{\partial x_L} = \sum_{j=-4N}^{4N} \mathbf{K}_L(\mu, j)\left\{[\mathbf{R}\overline{\mathbf{E}} - \overline{\overline{\mathbf{E}}}]\frac{\partial \mathbf{s}_L(\tau)}{\partial x_L}\bigg|_{\tau=\tau_L} - \mathbf{R}_0\frac{F_0}{\pi}\exp(-\tau_L/\mu_0)\frac{\partial \tau}{\partial x_L}\bigg|_{\tau=\tau_L}\overline{\overline{\Xi}}\right\}_j + \delta_{1L}\frac{\partial \mathbf{s}_1(\mu)}{\partial x_L} - \sum_{j=-4N}^{4N} \mathbf{K}_L(\mu, j)\left\{[\overline{\overline{\mathbf{E}}} - \mathbf{R}\overline{\mathbf{E}}]\left[\frac{\partial}{\partial x_L}\exp[\mathbf{A}_L(\tau - \tau_{L-1})]\right]\bigg|_{\tau=\tau_L}\mathbf{c}_L\right\}_j. \tag{21b}$$

In Eq. (21), the derivatives of the source term ($\mathbf{s}$) and the composite phase matrix ($\mathbf{A}$) on the right-hand side can be analytically derived from Eqs. (10)–(12) if x_l is set for the optical thickness and single scattering albedo. Thus, Jacobians including $\partial \mathbf{I}_1(\mu)/\partial \tau_l$ and $\partial \mathbf{I}_1(\mu)/\partial \varpi_l$ are analytic in form and can be computed very efficiently.

The Jacobian associated with the phase matrix variation may be derived if the angular dependence of all elements can be characterized in terms of the optical parameters. For example, in the phase function, the asymmetry parameter is introduced and used to characterize the angular distribution in the two-stream approximation. However, for a polarized two-stream approach, two additional parameters including phase polarization and asymmetry factors must be introduced so that the errors in the polarization forward modeling can be substantially reduced (Liu and Weng 2002). Thus, the Jacobian of the asymmetry parameter (g) can be directly computed from Eq. (21) (note that matrix $\mathbf{A}$ is analytically related to g). However, the derivation of the Jacobians relative to the general phase matrix remains difficult.

The Jacobians relative to the surface parameters (e.g., temperature and wind speed) can be derived as

$$\frac{\partial \mathbf{I}_1(\mu)}{\partial x_s} = \sum_{j=1}^{4N} \mathbf{K}_L(\mu, j)\left[B(T_s)\frac{\partial \boldsymbol{\epsilon}}{\partial x_s} + \frac{\partial B(T_s)}{\partial x_s}\boldsymbol{\epsilon} + \frac{\partial \mathbf{R}}{\partial x_s}\overline{\mathbf{E}}\mathbf{s}_L(\tau_L) + \frac{\partial \mathbf{R}_0}{\partial x_s}\frac{F_0}{\pi}\exp\left(-\frac{\tau_L}{\mu_0}\right)\overline{\overline{\Xi}}\right]_j + \sum_{j=1}^{4N} \mathbf{K}_L(\mu, j)\left\{\frac{\partial \mathbf{R}}{\partial x_s}\overline{\mathbf{E}}\exp[\mathbf{A}_L(\tau_L - \tau_{L-1})]\mathbf{c}_L\right\}_j. \tag{22}$$

Thus, the radiance gradient relative to other physical parameters can be directly deduced from Eq. (21). For example, the Jacobian of water vapor mixing ratio is

$$\frac{\partial \mathbf{I}_1(\mu)}{\partial q_l} = \frac{\partial \tau_l}{\partial q_l}\frac{\partial \mathbf{I}_1(\mu)}{\partial \tau_l} + \frac{\partial \varpi_l}{\partial q_l}\frac{\partial \mathbf{I}_1(\mu)}{\partial \varpi_l} = \kappa_l^{\text{abs}}\left[\frac{\partial \mathbf{I}_1(\mu)}{\partial \tau_l} - \frac{\varpi_l}{\tau_l}\frac{\partial \mathbf{I}_1(\mu)}{\partial \varpi_l}\right], \tag{23}$$

where q_l and κ_l^{abs} are the integrated water vapor (kg m^{-2}) and the mass absorption coefficient (m^2 kg^{-1}) of the water vapor at layer l, respectively. By the same

Table 1. Stokes vectors at the top of the atmosphere calculated from the VDISORT and compared with the results from the doubling–adding model for the L13 problem. The radiances are shown as a function of a cosine of zenith angle (μ) with a fixed solar zenith angle of 60° and a relative azimuth angle of 30°. The underlying surface is a Lambertian type with an albedo of 0.4.

	Doubling–adding				VDISORT			
μ	I	Q	U	V	I	Q	U	V
1.000 00	0.133 99	−0.009 81	0.016 99	0.000 00	0.133 99	−0.009 87	0.017 09	0.000 00
0.969 57	0.140 60	−0.016 60	0.022 86	0.000 03	0.140 60	−0.016 61	0.022 86	0.000 03
0.899 20	0.152 95	−0.021 65	0.028 93	0.000 03	0.152 95	−0.021 65	0.028 93	0.000 03
0.792 01	0.174 53	−0.025 61	0.036 52	0.000 01	0.174 53	−0.025 62	0.036 53	0.000 01
0.652 39	0.210 04	−0.027 63	0.045 99	−0.000 03	0.210 04	−0.027 63	0.046 00	−0.000 02
0.486 06	0.266 48	−0.026 32	0.057 42	−0.000 06	0.266 48	−0.026 32	0.057 42	−0.000 06
0.299 83	0.351 93	−0.020 23	0.070 00	−0.000 06	0.351 93	−0.020 23	0.070 00	−0.000 06
0.101 33	0.462 94	−0.011 02	0.079 99	0.000 07	0.462 94	−0.011 03	0.079 99	0.000 07

L13 problem (Garcia and Siewert 1989; Evans and Stephens 1991):

Wavelength: 0.951 μm; single layer of scattering media; gamma distribution of particles; effective radius: 0.2 μm; effective variances: 0.07; index of refraction $n = 1.44$; optical depth: 1.0; single scattering albedo: 0.99; surface albedo: 0.4; solar zenith angle: 60°; relative azimuth angle: 30°.

token, the Jacobian of cloud liquid water can be derived as

$$\frac{\partial \mathbf{I}_1(\mu)}{\partial w_l} = \frac{\partial \tau_l}{\partial w_l}\frac{\partial \mathbf{I}_1(\mu)}{\partial \tau_l} + \frac{\partial \varpi_l}{\partial w_l}\frac{\partial \mathbf{I}_1(\mu)}{\partial \varpi_l} = \frac{\tau_l - \kappa_l^{\text{abs}} q_l}{w_l}\frac{\partial \mathbf{I}_1(\mu)}{\partial \tau_l} + \frac{\varpi_l \kappa_l^{\text{abs}} q_l}{w_l \tau_l}\frac{\partial \mathbf{I}_1(\mu)}{\partial \varpi_l}, \quad (24)$$

where w_l is the integrated cloud liquid water within layer l. Furthermore, the temperature Jacobian is

$$\frac{\partial \mathbf{I}_1(\mu)}{\partial T_l} = \frac{\partial \mathbf{I}_1(\mu)}{\partial B(T_l)}\frac{\partial B(T_l)}{\partial T_l} + \frac{\partial \tau_l}{\partial T_l}\frac{\partial \mathbf{I}_1(\mu)}{\partial \tau_l} + \frac{\partial \varpi_l}{\partial T_l}\frac{\partial \mathbf{I}_1(\mu)}{\partial \varpi_l} = \frac{\partial \mathbf{I}_1(\mu)}{\partial BT_l}\frac{\partial B(T_l)}{\partial T_l} + q_l \frac{\partial \kappa_l^{\text{abs}}}{\partial T_l}\left[\frac{\partial \mathbf{I}_1(\mu)}{\partial \tau_l} - \frac{\varpi_l}{\tau_l}\frac{\partial \mathbf{I}_1(\mu)}{\partial \varpi_l}\right], \quad (25)$$

where the derivative of the absorption coefficient relative to temperature is generally negligible at visible wavelengths while that at thermal wavelengths can be either analytically derived or numerically evaluated. Thus, it is obvious that these Jacobians can be readily derived from a linear combination of those Jacobians relative to the optical thickness and single scattering albedo. Resulting computation efforts are optimally designed.

3. Simulation results

a. Forward model performance

In this section, the radiances computed from the present model are compared with those from the doubling-adding model (Evans and Stephens 1991). The first comparison is made for a typical L13 problem that uses a phase function for Mie scattering at a wavelength of 0.951 μm from a gamma distribution of particles with 0.2-μm effective radius, 0.07 effective variances, and index of refraction $n = 1.44$ (Garcia and Siewert 1989). The optical thickness and single scattering albedo are set as 1.0 and 0.99, respectively. The radiances are computed at various zenith angles for a collimated beam source at a solar zenith angle of 60° and a relative azimuth angle of 30° with a Mie phase matrix. The Legendre-series coefficients of the phase matrix [see Eq. (9)] were converted from the scattering coefficients (Garcia and Siewert 1989) in the study of Evans and Stephens (1991). The underlying surface is unpolarized and has an albedo of 0.4.

In the second case, the brightness temperatures at 37 GHz are computed from the VDISORT and the doubling–adding models for a nonprecipitating atmosphere. The atmosphere ranges from 0 to 8 km and is divided into three layers, including a cloud layer between 3 and 4 km (see Table 2 for detailed parameters). In each layer, the thermal source term in terms of Planck's function linearly varies with the optical thickness. The parameters such as optical thickness, single scattering albedo, and phase matrix within the cloudy layer are obtained from Mie calculations. Since the cloud droplets are spherical, the thermal source is essentially unpolarized. However, the underlying surface is a fully polarized and has an emissivity vector and a reflectivity matrix computed from an ocean polarimetric emissivity model (St. Germain and Poe 1998). These parameters are computed at the surface wind speed of 10 m s^{-1} and the surface temperature of 300 K.

Tables 1 and 2 list and compare the Stokes vectors computed from two models for both above cases. For the L13 problem, the results agree to the fourth to fifth decimal places at most viewing angles. For the microwave case, the discrepancies between the two models are less than 0.01 K for the first two Stokes components, whereas the results are identical for the third and fourth components. Thus, the forward model calculations including beam and thermal sources, scattering and surface polarization are reliable and accurate.

It is important to know that the atmospheric constit-

Table 2. Stokes vectors at the top of the atmosphere calculated from the VDISORT and compared with the results from the doubling–adding model for a microwave frequency of 37 GHz. The radiances are converted to brightness temperatures and shown as a function of the relative azimuthal angle (ϕ) between the viewing direction and wind direction with a fixed zenith angle of 53°. Ocean surface emissivity vector is calculated from the polarimetric model with a wind speed of 10 m s^{-1}.

	Doubling–adding				VDISORT			
ϕ	I	Q	U	V	I	Q	U	V
0	228.599	32.371	0.000	0.000	228.604	32.367	0.000	0.000
15	228.385	32.088	−0.671	0.148	228.390	32.083	−0.671	0.148
30	227.846	31.343	−1.172	0.258	227.851	31.339	−1.172	0.258
45	227.231	30.403	−1.391	0.299	227.237	30.398	−1.391	0.299
60	226.799	29.575	−1.309	0.259	226.805	29.571	−1.309	0.259
75	226.678	29.080	−0.997	0.146	226.684	29.076	−0.997	0.146
90	226.802	28.976	−0.578	−0.010	226.808	28.972	−0.578	−0.010
105	226.966	29.161	−0.182	−0.170	226.971	29.157	−0.182	−0.170
120	226.950	29.458	0.102	−0.290	226.956	29.454	0.102	−0.290
135	226.663	29.712	0.238	−0.335	226.668	29.708	0.238	−0.335
150	226.193	29.853	0.239	−0.291	226.198	29.849	0.239	−0.291
165	225.759	29.900	0.143	−0.168	225.765	29.896	0.143	−0.168
180	225.584	29.906	−0.000	0.000	225.590	29.902	0.000	−0.000
195	225.759	29.900	−0.143	0.168	225.765	29.896	−0.143	0.168
210	226.193	29.853	−0.239	0.291	226.198	29.849	−0.239	0.291
225	226.663	29.712	−0.238	0.335	226.668	29.708	−0.238	0.335
240	226.950	29.458	−0.102	0.290	226.956	29.454	−0.102	0.290
255	226.966	29.161	0.182	0.170	226.971	29.157	0.182	0.170
270	226.802	28.976	0.578	0.010	226.808	28.972	0.578	0.010
285	226.678	29.080	0.997	−0.146	226.684	29.076	0.997	−0.146
300	226.799	29.575	1.309	−0.259	226.805	29.571	1.309	−0.259
315	227.231	30.403	1.391	−0.299	227.237	30.398	1.391	−0.299
330	227.846	31.343	1.172	−0.258	227.851	31.339	1.172	−0.258
345	228.385	32.088	0.671	−0.148	228.390	32.083	0.671	−0.148
360	228.599	32.371	−0.000	0.000	228.604	32.367	0.000	−0.000

Microwave problem:

Frequency: 37 GHz; atmosphere stratification: 3 layers gamma size distribution of cloud droplets; effective radius: 10 μm; liquid waterpath (3–4 km): 0.5 mm; surface temperature: 300 K; surface wind speed: 10 m s^{-1}; local zenith angle: 53°.

245 K ..... 8 km
vapor
273 K ..... 4 km
vapor and cloud
280 K ..... 3 km
vapor
300 K ..... 0 km

uents in the above two cases modify the polarization source through different processes. In the L13 problem, the polarization information in Q, U, and V components result from the multiple scattering that redistributes the radiation from the unpolarized beam source, whereas in the microwave problem, the polarization signals arise primarily from the ocean emission that is fully polarimetric. Atmospheric gases and cloud hydrometeors in the second case mainly attenuate the surface polarization and thermally emit unpolarized radiation.

b. Jacobian model performance

In theory, the Jacobians corresponding to various geophysical parameters can be calculated using the finite differential method (FDM) that computes the radiance twice with one relative to the basic state and the other corresponding to the perturbed condition. In this approach, a perturbation to the parameter within a layer requires new calculations of all the optical parameters at other layers; thus, the technique demands huge computational resources. Furthermore, the perturbation to each parameter should be small, but large enough to produce a meaningful radiance perturbation. Strictly speaking, the ratio of radiance perturbation to the variable increment approaches the actual gradient when the increment approaches zero. In general, there is no criterion for selecting the perturbation magnitude. Thus, there is always an uncertainty in using the FDM for the radiance gradient calculation.

To illustrate how the FDM converges with the VDISORT Jacobian model, we compute and compare the Jacobians relative to the various parameters under a cloudy atmosphere where the hydrometeors in various phases coexist. The atmospheric profiles including temperature, water vapor, cloud liquid, ice, and rainwater contents are the outputs of the fifth-generation Pennsylvania State University (PSU)–National Center for Atmospheric Research (NCAR) Mesoscale Model (MM5) simulations of Hurricane Bonnie (see Fig. 1). Note that only cloud liquid and ice water contents (nonprecipitating components) are used to compute the Jacobians at 0.67 μm because they occur higher in the atmosphere and first interact effectively with solar radiation. At 37 GHz, both cloud liquid (nonprecipitating) and rainwater (precipitating) contents are used because ice clouds are

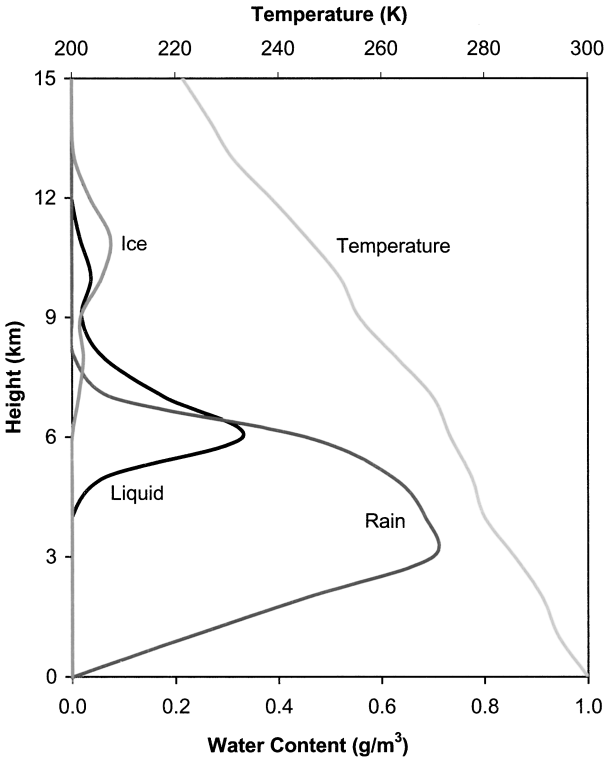

FIG. 1. Vertical distributions of temperature, cloud liquid, and ice water content contributed from nonprecipitating hydrometers, and rainwater content from precipitating hydrometers.

relatively transparent and their radiative effects can be neglected at this frequency. Tables 3 and 4 display the mean single scattering albedo and optical thickness at 0.67 μm and 37 GHz, respectively, from Mie calculations. A general gamma-sized distribution function is used with an effective radius of 10 μm for nonraining clouds and 500 μm for raining clouds. As shown in Table 3, while the single scattering albedo at 0.67 μm varies between 0.9 and 1.0, the optical thickness displays the largest peak in between 6- and 7-km altitudes and is associated with the peak of the cloud liquid water content. At 37 GHz, both the optical thickness and single scattering albedo vary significantly with altitude and peak between 3 and 4 km where the rainwater content is maximal. However, a maximum of single scattering albedo is only 0.38, which indicates the scattering is not a predominate process.

Tables 5 and 6 display the ratio of the Jacobians of the optical thickness derived from the VDISORT to those from the FDM at 0.67 μm and 37 GHz, respectively. At a smaller $\Delta\tau$ of 0.01, the Jacobian ratio approaches unity for all four components throughout most of the atmosphere. At 37 GHz, $\Delta\tau$ of 0.001 may be needed for the FDM to obtain an accuracy approaching that from the VDISORT. For the same $\Delta\tau$ of 0.01 (see Tables 5 and 6), the Jacobian caclculations at a larger optical thickness at 0.67 μm converge much faster than those at a smaller one at 37 GHz. This again illustrates

Table 3. Optical thickness and single scattering albedo at 0.67 μm for cloud liquid and ice profiles as shown in Fig. 1.

Layer (km)	Single scattering albedo	Optical thickness
14–15	0.937 91	0.0015
13–14	0.999 37	1.1707
12–13	0.999 82	1.0520
11–12	0.999 91	3.5874
10–11	0.999 94	5.0062
9–10	0.999 92	2.2034
8–9	0.999 97	6.0687
7–8	0.999 99	16.3954
6–7	0.999 99	29.5249
5–6	0.999 95	5.8143
4–5	0.958 24	0.0089
3–4	0.983 05	0.0171
2–3	0.995 70	0.0289
1–2	0.997 03	0.0444
0–1	0.996 54	0.0465

that the perturbation used in the FDM must be small but large enough relative to the basic state so that the radiance perturbation is computed to be numerically meaningful. Table 7 displays the ratio of the Jacobians of the single scattering albedo derived from the VDISORT to those from the FDM at 37 GHz. It shows that the two methods agree well.

c. *Jacobian profiles of clouds*

The VDISORT Jacobian model is further utilized to compute various Jacobian profiles. Figures 2a and 2b display the profiles of the Jacobians at 0.67 μm relative to the optical thickness and single scattering albedo, respectively. Here, four Stokes components should be interpreted as the gradients of the cloud reflectance relative to the optical parameters. In particular, the Jacobian of the optical thickness is negative for the I component and positive for the Q component near the cloud top (see Fig. 2a), which implies that an increase of the optical thickness there tends to reduce the cloud reflectance and increase the polarization. The smallest Ja-

Table 4. Optical thickness and single scattering albedo at 37 GHz for cloud liquid and rainwater profiles.

Layer (km)	Single scattering albedo	Optical thickness
14–15	0.000 00	0.000 40
13–14	0.000 00	0.000 60
12–13	0.000 00	0.000 70
11–12	0.000 00	0.001 00
10–11	0.000 04	0.008 90
9–10	0.000 05	0.018 70
8–9	0.000 05	0.011 20
7–8	0.003 13	0.028 70
6–7	0.096 86	0.119 30
5–6	0.289 51	0.611 80
4–5	0.358 88	0.764 50
3–4	0.375 52	0.838 50
2–3	0.375 12	0.865 30
1–2	0.328 77	0.554 10
0–1	0.295 11	0.219 40

Table 5. The ratio of the optical thickness Jacobian at 0.67 μm computed from the present method to that from the finite differential method, as a function of an increment of the optical thickness. The profiles of cloud liquid and ice water content shown in Fig. 1 and optical parameters listed in Table 3 are used in computations.

	$\Delta\tau = 0.1$				$\Delta\tau = 0.01$			
Z (km)	I	Q	U	V	I	Q	U	V
15	1.060	0.634	1.372	0.907	1.007	0.959	1.041	0.991
14	1.061	0.658	2.228	0.900	1.007	0.962	1.136	0.990
13	1.030	1.091	0.979	1.000	1.004	1.010	0.996	1.000
12	1.016	1.001	1.062	1.000	1.002	0.996	0.996	1.000
11	0.999	1.041	1.000	1.000	1.000	1.000	1.000	1.000
10	0.999	1.035	1.000	1.000	1.000	1.000	1.000	1.000
9	0.999	1.038	1.000	1.000	1.000	1.000	1.000	1.000
8	0.999	1.031	1.000	1.000	1.000	1.000	1.000	1.000
7	0.999	1.030	1.000	1.000	1.000	1.000	1.000	1.000
6	0.999	1.030	1.000	1.000	1.000	1.000	1.000	1.000
5	0.999	1.030	1.000	1.000	1.000	1.000	1.000	1.000
4	1.354	1.000	1.000	1.000	1.041	1.000	1.000	1.000
3	0.982	1.036	1.000	1.000	0.998	0.998	1.000	1.000
2	0.996	1.031	1.000	1.000	1.000	1.000	1.000	1.000
1	0.997	1.031	1.000	1.000	1.000	1.000	1.000	1.000

cobians within the cloud indicate negligible sensitivity of the reflectance to the optical thickness. On the other hand, the Jacobians of the single scattering albedo vary significantly within the cloud (see Fig. 2b). Note that the Jacobian is maximal for I component and minimal for Q component at 11 km where the cloud ice water content peaks. Furthermore, the Jacobians in U and V components vary with height but peak above the maximum of the cloud ice water content.

Figures 3a and 3b display the Jacobians at 37 GHz relative to cloud liquid water and rainwater content, respectively. The Jacobian in I component is positive whereas that in Q component is slightly negative (see Fig. 3a). This implies that nonprecipitating cloud emits the radiation at this frequency and results in an increase in the brightness temperatures as the cloud liquid content increases. However, for precipitating clouds (see Fig. 3b), the Jacobian is initially positive between 7 and 9 km and then becomes largely negative between 3 and 6 km. This is due to the emission from a small amount of the raining droplets aloft and the scattering from the large raindrops at lower levels. The positive Jacobian in the Q component at the lower levels results from the scattering of larger raindrops.

4. Microwave emissivity model performance

For completeness in describing the radiative transfer model in the satellite data assimilation, microwave emissivity models over land and ocean are summarized in this section.

a. Land emissivity model

Both radiance and Jacobian computations require knowledge of surface emissivity and reflectivity. Pres-

Table 6. The ratio of the optical thickness Jacobian at 37 GHz computed from the present method to that from the finite differential method, as a function of an increment of the optical thickness. The profiles of the cloud liquid and rainwater content shown in Fig. 1 and optical parameters listed in Table 4 are used in computations.

	$\Delta\tau = 0.1$		$\Delta\tau = 0.01$		$\Delta\tau = 0.001$	
Z (km)	I	Q	I	Q	I	Q
15	0.988	0.994	0.994	0.997	0.993	0.994
14	1.003	0.995	0.996	0.997	0.994	0.994
13	1.035	0.997	1.000	0.998	0.994	0.994
12	1.114	0.999	1.010	0.998	0.995	0.994
11	1.416	1.001	1.047	0.998	0.999	0.994
10	−2.909	1.003	0.513	0.999	0.944	0.994
9	0.531	1.004	0.938	0.999	0.988	0.994
8	0.734	1.008	0.963	0.999	0.990	0.994
7	0.785	1.008	0.969	0.999	0.991	0.994
6	0.809	0.956	0.972	0.991	0.991	0.993
5	1.024	0.888	0.997	0.982	0.994	0.992
4	0.946	−5.059	0.988	0.346	0.993	0.928
3	0.945	0.972	0.988	0.991	0.993	0.993
2	0.941	0.955	0.988	0.989	0.993	0.993
1	0.955	0.954	0.989	0.989	0.993	0.993

Table 7. The ratio of the single scattering albedo Jacobian at 37 GHz computed from the present method to that from the finite differential method, as a function of an increment of the single scattering albedo. The profiles of cloud liquid and rainwater content shown in Fig. 1 and optical parameters listed in Table 4 are used in computations.

	$\Delta\varpi = 0.1$		$\Delta\varpi = 0.001$	
Z (km)	I	Q	I	Q
10	0.995	0.943	0.993	0.993
9	0.997	0.955	0.993	0.993
8	0.995	0.979	0.993	0.993
7	0.998	0.970	0.993	0.993
6	1.011	0.957	0.994	0.993
5	1.052	0.976	0.994	0.993
4	1.065	1.005	0.994	0.993
3	1.069	1.021	0.994	0.994
2	1.068	1.033	0.994	0.994
1	1.054	1.030	0.994	0.994

ently, these quantities can only be simulated at selected frequencies and under limited surface conditions. For a vector radiative transfer modeling, the emissivity is needed in the form of a vector and the reflectivity is determined as a matrix having 16 elements (Weng 1992). At microwave frequencies, a model for simulating the land emissivity over various surface conditions was developed (Weng et al. 2001). For surfaces such as snow, desert, and vegetation, volumetric scattering was calculated using a two-stream radiative transfer approximation. In the case of vegetation, geometrical optics are used since the leaf size is typically larger than the wavelength. For snow and deserts, a dense medium theory was adopted to take into account the coherent scattering by closely spaced particles.

Figures 4a and 4b display the emissivity spectra obtained from the land emissivity model (Weng et al. 2001). The emissivity of ocean surfaces is also shown for a comparison. The emissivity of snow decreases as frequency increases due to the scattering from snow particles. The characteristics of wetland emissivity are similar to those over oceans in that the emissivity increases and the polarization decreases as the frequency increases. However, the emissivity spectra of other land surfaces do not exhibit a large variability in most of the frequency range. Thus, the uncertainty in simulating land emissivity is the largest over snow-covered and desert regions where an assessment of the dense medium scattering is still problematic.

b. Ocean emissivity model

For ocean surfaces, the model was developed to simulate the emissivity vector using a two-scale ocean roughness approximation (Yueh 1997). The emission from large-scale waves is normally polarimetric and is modeled by the geometrical optics (GO) scattering theory (Stogryn 1967). In the GO model, the large-scale waves are modeled by tilting surface facets, and the scattering coefficients are proportional to the number of surface facets with a sloping angle satisfying the specular reflection condition. The slope distribution of the

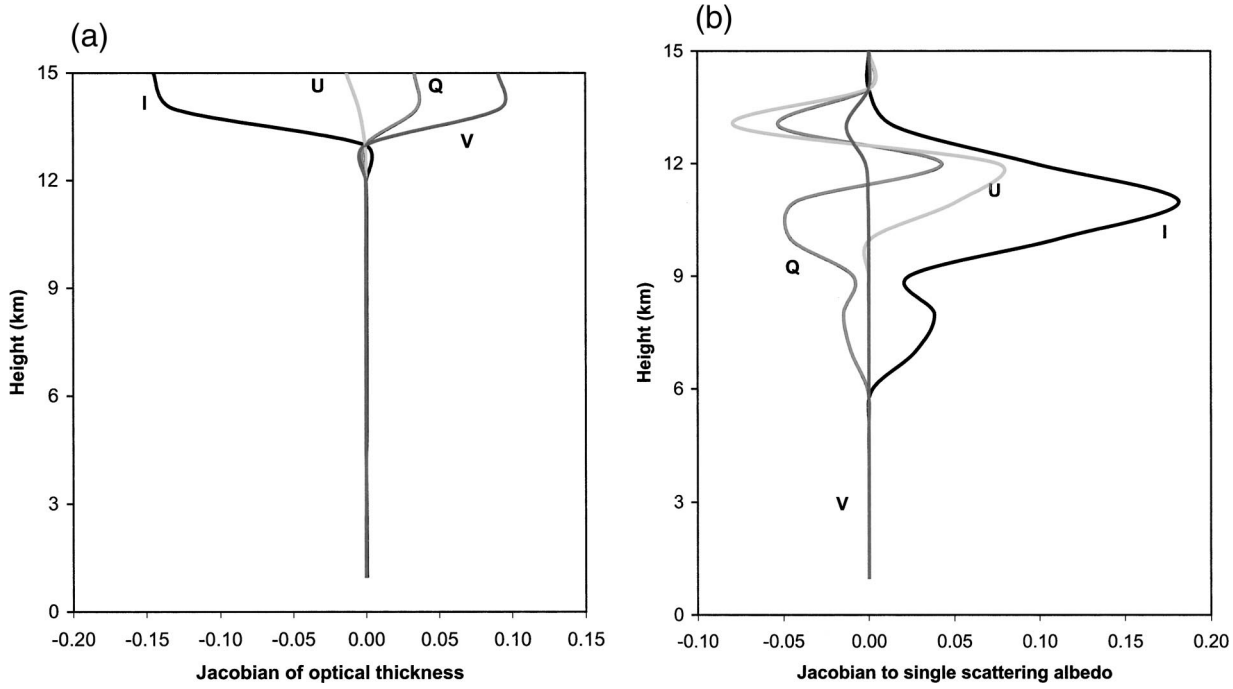

FIG. 2. (a) Vertical distribution of Jacobians of optical thickness at 0.67 μm. The values of Q and U are multiplied by a factor of 10^3, and the value of V is multiplied by a factor of 10^5. (b) Vertical distribution of Jacobians of single scattering albedo at 0.67 μm. The value of I is divided by a factor of 10. The values of Q and U are multiplied by a factor of 10^2, and the value of V is multiplied by a factor of 10^3.

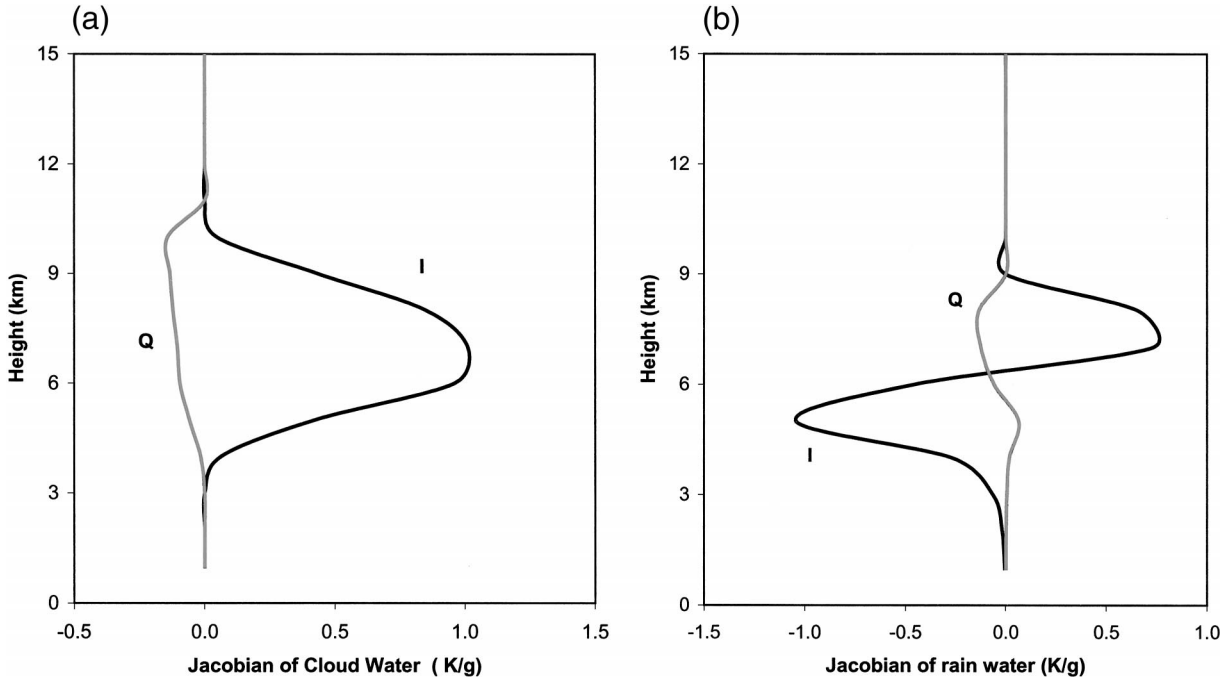

FIG. 3. Vertical distributions of Jacobians of (a) cloud liquid water and (b) rainwater. Note that both Jacobians are divided by a factor of 10.

large-scale roughness is computed from an ocean surface spectrum (Cox and Munk 1954; Durden and Vesecky 1985). However, the GO scattering theory underestimates the directional signals in the first three components of the emissivity vector and predicts no signals in the fourth component (Gasiewski and Kunkee 1994). Bragg scattering from the small-scale waves was found to be useful in explaining the dependence of the emissivity on ocean wind direction and the existence of the fourth component in the emissivity vector (Yueh 1997). The cutoff wavenumber for separating between the large- and small-scale waves depends on frequency and can be optimally derived (Liu et al. 1998).

The polarimetric emission and reflection components are simulated over oceans using the two-scale model as described above and the results of the simulations are expressed in terms of the brightness temperatures. As previously demonstrated, the brightness temperature difference between vertical and horizontal polarization states can be related to the surface wind speed (e.g., Goodberlet et al. 1989; Wentz 1992). The third and fourth Stokes components are primarily dependent on the surface wind direction (Yeuh et al. 1994; Yueh 1997). Figures 5a and 5b display the third and fourth components as a function of the relative azimuthal angle at various microwave frequencies. The relative azi-

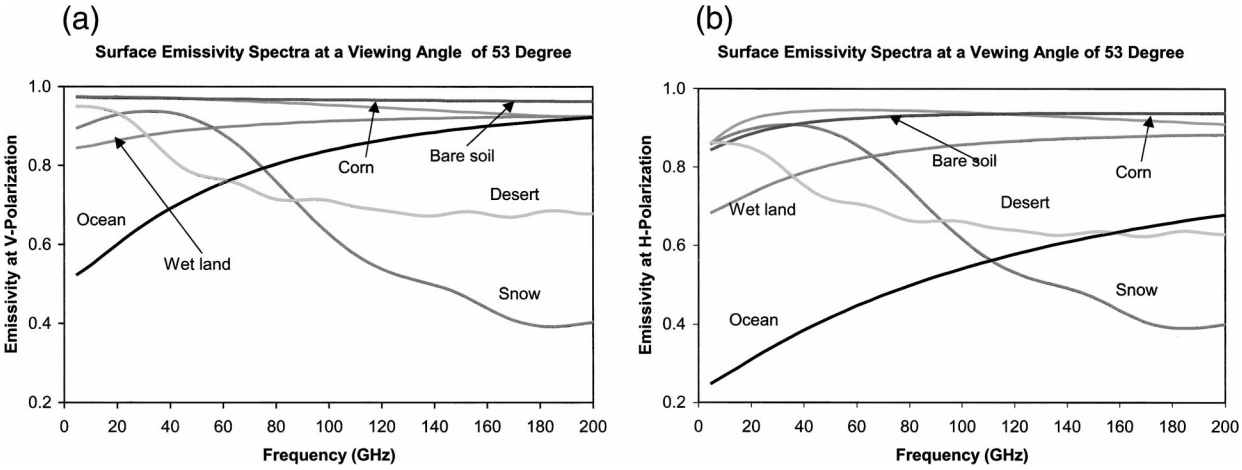

FIG. 4. Land emissivity spectra for various surfaces at (a) v polarization and (b) h polarization.

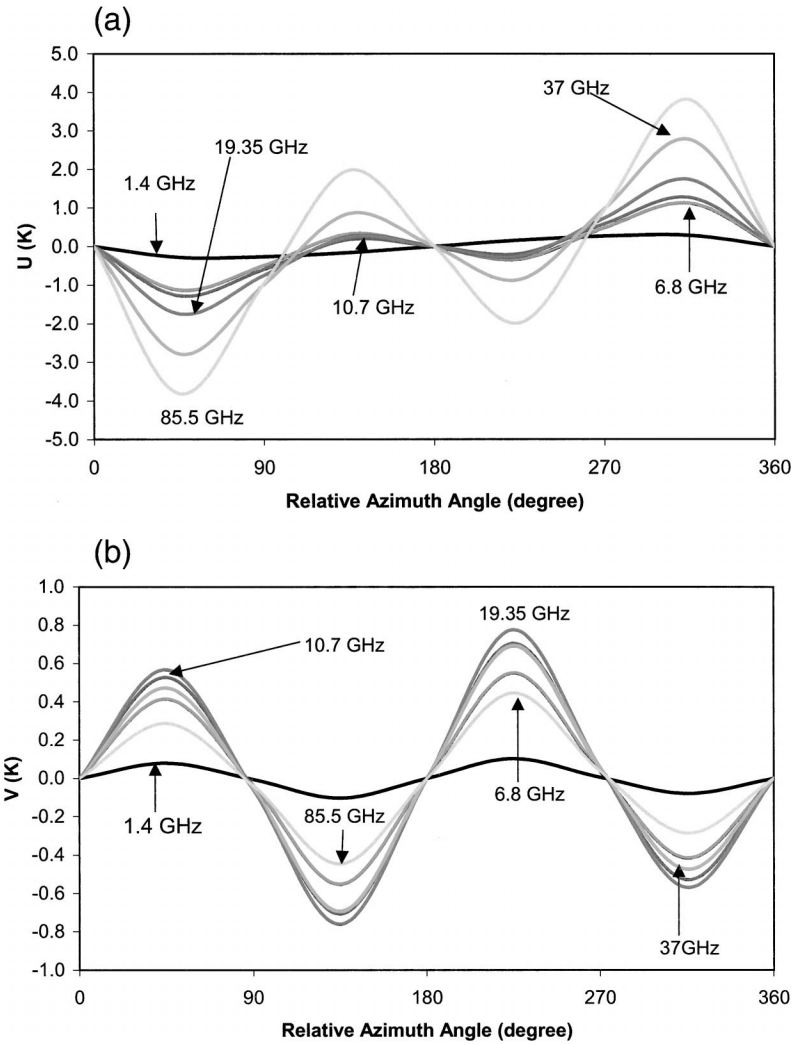

FIG. 5. Polarimetric brightness temperatures simulated from the two-scale emissivity model for a wind speed of 10 m s^{-1} at a 19.5-m height. (a) The third Stokes component vs relative azimuthal angle, and (b) the fourth Stokes component vs relative azimuthal angle.

muthal angle is the difference between the wind direction and the instrument look azimuth, both measured relative to geographic north. Here, U exhibits various harmonic components with an amplitude of a few degrees Kelvin at a wind speed of 10 m s^{-1}. The amplitude increases as frequency increases. Note also that U and V are out of phase and the amplitude of V is less than 1.0 K at this wind speed. These simulated results are consistent with those obtained from an aircraft radiometer (St. Germain and Poe 1998).

5. Summary and conclusions

The vector discrete-ordinate radiative transfer model (VDISORT) is enhanced to allow the most efficient and accurate computations of both radiance and Jacobians. In this model, the emission and scattering of clouds and polarization from both surface and atmosphere are explicitly taken into account. It is shown that the radiances calculated from the present scheme are accurate, compared to the results from the doubling–adding model. The Jacobians relative to various parameters are computed more accurately and faster than those from the finite differential method because they are all analytically related to the parameters at the basic state. In general, the VDISORT computes Jacobians 10 to 100 times faster than the finite differential method when all radiative processes such as scattering and polarization are included. The computational efficiency of the present model in deriving Jacobians varies, depending on various applications. For an atmosphere having 15 layers, the present model computes Jacobians with respect to optical thickness, single scattering albedo, and temperature 14 times faster than the finite differential tech-

nique. The computational resource will be saved even more significantly for additional Jacobians, for example, with respect to water vapor and cloud water mixing ratios. Thus, the methodology may be directly utilized in the satellite data assimilation under cloudy conditions.

In the satellite data assimilation, the modeling of surface radiative properties such as emissivity and reflectivity is an important issue and is reviewed in this study. The various emissivity models are being integrated as part of the radiative transfer and Jacobian models. The emissivity models are developed over several surface conditions due to an improved understanding in the electromagnetic wave theory at microwave frequencies. Over oceans, a full polarimetric emissivity model is proposed and validated against the aircraft measurements. Over land, the microwave land emissivity model is used to compute the various emissivity spectra and is being implemented into the operational data assimilation system.

Acknowledgments. This study was supported through the funding from NOAA/Integrated Program Office, and the Joint Center for Satellite Data Assimilation.

APPENDIX A

Decoupling Azimuth Angles

In a vector radiative transfer problem, one often uses Fourier harmonic expansion to represent the variable components so that the integration term in the equation can be discretized. In doing so, we first express

$$\mathbf{M}(\tau, \mu, \phi; \mu', \phi') = \sum_{m=0}^{N} \left[\frac{\mathbf{M}_m^c(\tau, \mu, \mu')}{1 + \delta_{0m}} \cos m(\phi' - \phi) + \mathbf{M}_m^s(\tau, \mu, \mu') \sin m(\phi' - \phi) \right], \quad \text{(A1)}$$

$$\mathbf{I}(\tau, \mu, \phi) = \sum_{m=0}^{N} [\mathbf{I}_m^c(\tau, \mu) \cos m(\phi_0 - \phi') + \mathbf{I}_m^s(\tau, \mu) \sin m(\phi_0 - \phi')], \quad \text{(A2)}$$

$$\mathbf{S}(\tau, \mu, \phi) = \sum_{m=0}^{N} [\mathbf{S}_m^c(\tau, \mu) \cos m(\phi_0 - \phi') + \mathbf{S}_m^s(\tau, \mu) \sin m(\phi_0 - \phi')], \quad \text{(A3)}$$

where δ_{0m} is the Kronecker delta.

The phase matrix $\mathbf{M}$ has some special properties. For spherical particles or randomly oriented nonspherical particles, the submatrix off its diagonal elements has nonzero elements in Fourier sinusoidal harmonics, whereas the submatrix in the diagonal has nonzero elements in the consinusoidal harmonics (Evens and Stephens 1991; Weng 1992; Schulz et al. 1999). By substituting Eqs. (A1)–(A3) into Eqs. (3a)–(3b), and comparing the cosine and sine harmonics between both sides of the equation (Evans and Stephens 1991), we obtain

$$\mu \frac{d\mathbf{I}_m(\tau, \mu)}{d\tau} = -\mathbf{I}_m(\tau, \mu) + \varpi \int_0^1 \mathbf{M}_m(\mu, \mu')\mathbf{I}_m(\tau, \mu')\, d\mu' + \varpi \int_0^1 \mathbf{M}_m(\mu, -\mu')\mathbf{I}_m(\tau, -\mu')\, d\mu' + \mathbf{S}_m, \quad \text{(A4)}$$

where

$$\mathbf{I}_m = [I_m^c, Q_m^c, U_m^s, V_m^s]^{\mathrm{T}}, \quad \text{(A5)}$$

$$\mathbf{S}_m = [S_m^c, S_m^c, S_m^s, S_m^s]^{\mathrm{T}}, \quad \text{(A6)}$$

$$\mathbf{M}_m = \begin{bmatrix} M_{11m}^c & M_{12m}^c & M_{13m}^s & M_{14m}^s \\ M_{21m}^c & M_{22m}^c & M_{23m}^s & M_{24m}^s \\ -M_{31m}^s & -M_{32m}^s & M_{33m}^c & M_{34m}^c \\ -M_{41m}^s & -M_{42m}^s & M_{43m}^c & M_{44m}^c \end{bmatrix}. \quad \text{(A7)}$$

In theory, there is another set for a combined radiance vector similar to (A5), which includes the sinusoidal part as the first two components and the cosine part as the third and fourth components. However, the solution is null since the solar and thermal source are even functions and unpolarized. Even for a rough ocean surface, the emitted thermal source has only the components of (A5) (Yueh 1997).

Replacing the integration in Eq. (A4) by a discrete sum and omitting the superscripts, one can obtain Eq. (4) in the main text.

APPENDIX B

Expression of Exponential Functions of Matrix

According to the definition, the matrix $\mathbf{A}$ can be expressed as

$$\mathbf{A} = \mathbf{g}\boldsymbol{\lambda}\mathbf{g}^{-1}, \quad \text{(B1)}$$

where $\mathbf{g}$ is an eigenvector matrix, $\boldsymbol{\lambda}$ is a diagonal matrix, and its elements are eigenvalues.

Using Taylor expansion, one may expand the exponential matrix as

$$\exp(\mathbf{A}\tau) = \sum_{k=0}^{\infty} \frac{(A\tau)^k}{k!}. \quad \text{(B2)}$$

For small optical thickness, one needs only to keep the first few terms in Eq. (B2). For large optical thickness, Eq. (2) can be rewritten by applying Eq. (B1) as

$$\exp(\mathbf{A}\tau) = \sum_{k=0}^{\infty} \frac{(\mathbf{A}\tau)^k}{k!} = \sum_{k=0}^{\infty} \frac{(\mathbf{g}\boldsymbol{\lambda}\mathbf{g}^{-1}\tau)^k}{k!} = \mathbf{g}\left[\sum_{k=0}^{\infty} \frac{(\boldsymbol{\lambda}\tau)^k}{k!}\right]\mathbf{g}^{-1} = \mathbf{g} \exp(\boldsymbol{\lambda}\tau)\mathbf{g}^{-1}. \quad \text{(B3)}$$

For the matrix having a size of N by N, Eq. (B3) can be expressed as

$$\exp(\mathbf{A}\tau) = \begin{bmatrix} g_{11} & \cdot & \cdot & g_{1n} \\ \cdot & \cdot & \cdot & \cdot \\ \cdot & \cdot & \cdot & \cdot \\ g_{n1} & \cdot & \cdot & g_{nn} \end{bmatrix} \begin{bmatrix} e^{\lambda_1\tau} & \cdot & \cdot & \cdot \\ \cdot & \cdot & \cdot & \cdot \\ \cdot & \cdot & \cdot & \cdot \\ \cdot & \cdot & \cdot & e^{\lambda_n\tau} \end{bmatrix} \begin{bmatrix} g_{11} & \cdot & \cdot & g_{1n} \\ \cdot & \cdot & \cdot & \cdot \\ \cdot & \cdot & \cdot & \cdot \\ g_{n1} & \cdot & \cdot & g_{nn} \end{bmatrix}^{-1}, \quad \text{(B4)}$$

which defines the properties needed in this improved radiative transfer model.

REFERENCES

Box, M. A., S. A. W. Gerstle, and C. Simmer, 1988: Application of the adjoint formation to the calculation of atmospheric radiative effects. *Beitr. Phys. Atmos.*, **61,** 301–311.

Cox, C. S., and W. H. Munk, 1954: Measurement of the roughness of the sea surface from photographs of the sun's glitter. *J. Opt. Soc. Amer.*, **44,** 838–850.

Durden, S. P., and J. F. Vesecky, 1985: Physical radar cross-section model for a wind-driven sea with swell. *IEEE J. Oceanic Eng.*, **OE-10,** 445–451.

Errico, R. M., 1997: What is an adjoint? *Bull. Amer. Meteor. Soc.*, **78,** 2577–2591.

Evans, K. F., and G. L. Stephens, 1991: A new polarized atmospheric radiative transfer model. *J. Quant. Spectrosc. Radiat. Transfer*, **46,** 413–423.

Eyre, J. R., 1989: Inversion of cloudy satellite sounding radiances by non-linear optimal estimation. I: Theory and simulation for TOVS. *Quart. J. Roy. Meteor. Soc.*, **115,** 1001–1026.

Garand, L., and Coauthors, 2001: Radiance and Jacobian intercomparison of radiative transfer models applied to HIRS and AMSU channels. *J. Geophys. Res.*, **106,** 24 017–24 031.

Garcia, R. D. M., and C. E. Siewert, 1989: A generalized spherical harmonics solution for radiative transfer models that include polarization effects. *J. Quant. Spectrosc. Radiat. Transfer*, **36,** 401–423.

Gasiewski, A. J., and D. B. Kunkee, 1994: Polarized microwave emission from water waves. *Radio Sci.*, **29,** 1449–1466.

Goodberlet, M. A., C. T. Swift, and J. C. Wilkerson, 1989: Remote sensing of ocean surface winds with the SSM/I. *J. Geophys. Res.*, **94,** 14 547–14 555.

Landgraf, J., O. P. Hasekamp, and T. Trautmann, 2002: Linearization of radiative transfer with respect to surface properties. *J. Quant. Spectrosc. Radiat. Transfer*, **72,** 327–339.

Liu, Q., and E. Ruprecht, 1996: A radiative transfer model: Matrix operator method. *Appl. Opt.*, **35,** 4229–4237.

——, and F. Weng, 2002: A microwave polarimetric two-stream radiative transfer model. *J. Atmos. Sci.*, **59,** 2402–2396.

——, C. Simmer, and E. Ruprecht, 1998: Monte Carlo simulations of the microwave emissivity of the sea surface. *J. Geophys. Res.*, **103,** 24 983–24 989.

Marchuk, G. I., 1964: Equation for the value of information from weather satellites and formulation of inverse problems. *Cosmic Res.*, **2,** 394–408.

Sendra, C., and M. A. Box, 2000: Retrieval of the phase function and scattering optical thickness of aerosols: A radiative perturbation theory application. *J. Quant. Spectrosc. Radiat. Transfer*, **64,** 499–515.

Shultz, F. M., and K. Stamnes, 2000: Angular distribution of the Stokes vector in a plane-parallel vertically inhomogeneous medium in the vector discrete ordinate radiative transfer (VDISORT) model. *J. Quant. Spectrosc. Radiat. Transfer*, **65,** 609–620.

——, ——, and F. Weng, 1999: An improved and generalized discrete ordinate radiative transfer model for polarized (vector) radiative transfer computations. *J. Quant. Spectrosc. Radiat. Transfer*, **61,** 105–122.

Spurr, R. J. D., T. P. Kurosu, and K. V. Chance, 2001: A linearized discrete ordinate radiative transfer model for atmospheric remote-sensing retrieval. *J. Quant. Spectrosc. Radiat. Transfer*, **68,** 689–735.

Stamnes K., S.-C. Tsay, W. Wiscombe, and K. Jayaweera, 1988: Numerically stable algorithm for discrete ordinate method radiative transfer in multiple scattering and emitting layered media. *Appl. Opt.*, **27,** 2502–2529.

St. Germain, K., and G. Poe, 1998: Polarimetric emission model of the sea at microwave frequencies, Part II: Comparison with measurements. Naval Research Laboratory Rep., Washington, D.C.

Stogryn, A., 1967: The apparent temperature of sea at microwave frequencies. *IEEE Trans. Antennas Propag.*, **AP-15,** 278–286.

Ustinov, E. A., 2001: Adjoint sensitivity analysis of radiative transfer equation: Temperature and gas mixing ratio weighting function for remote sensing of scattering atmospheres in thermal IR. *J. Quant. Spectrosc. Radiat. Transfer*, **68,** 195–211.

van Oss, R. F., and R. J. D. Spurr, 2002: Fast and accurate 4 and 6 stream linearized discrete ordinate radiative transfer models for ozone profile remote sensing retrieval. *J. Quant. Spectrosc. Radiat. Transfer*, **75,** 177–220.

Weng, F., 1992: A multi-layer discrete-ordinate method for vector radiative transfer in a vertically-inhomogeneous, emitting and scattering atmosphere—I: Theory. *J. Quant. Spectrosc. Radiat. Transfer*, **47,** 19–33.

——, B. Yan, and N. C. Grody, 2001: A microwave land emissivity model. *J. Geophys. Res.*, **106,** 20 115–20 123.

Wentz, F. J., 1992: Measurements of oceanic wind vector using satellite microwave radiometers. *IEEE Trans. Geosci. Remote Sens.*, **30,** 960–972.

Yueh, S. H., 1997: Modeling of wind direction signals in polarimetric sea surface brightness temperatures. *IEEE Trans. Geosci. Remote Sens.*, **35,** 1400–1418.

——, R. Kwok, F. K. Li, S. V. Nghiem, and W. J. Wilson, 1994: Polarimetric passive remote sensing of ocean wind vectors. *Radio Sci.*, **29,** 799–814.